International Journal of Fatigue 164 (2022) 107128

Contents lists available at ScienceDirect

International Journal of Fatigue

journal homepage: www.elsevier.com/locate/ijfatigue

Influence of pitting corrosion on the fatigue strength of offshore steel structures based on 3D surface scans

Sulaiman Shojai [a,*], Peter Schaumann [a], Moritz Braun [b], Sören Ehlers [b,c]

[a] Leibniz University Hannover, Institute for Steel Construction ForWind, Hannover, Germany
[b] Hamburg University of Technology, Institute for Ship Structural Design and Analysis, Hamburg, Germany
[c] German Aerospace Centre (DLR), Institute of Maritime Energy Systems, Geesthacht, Germany

ARTICLE INFO

Keywords:
Offshore-wind
Corrosion fatigue
Pitting corrosion
3D-Surface scan
Reverse engineering
Stress concentrations

ABSTRACT

Support structures for offshore wind turbines and the corresponding transformer platforms are highly susceptible to corrosion. In particular, the phenomenon of pitting is crucial, as it leads to local stress concentrations and thus affects the fatigue life of structures. Despite corrosion protection systems, corrosion cannot be completely avoided, which can lead to pitting corrosion on the steel surface. This leads to fatigue life reduction, since the structures are exposed to high dynamic loads. Local stress concentrations can be considered in local concepts but so far, corrosion effects in local concepts are insufficiently defined. Hence, this paper aims to investigate the impact of pitting corrosion and the corresponding stress concentration on the fatigue life endurance of structural steel, used for offshore wind support structures. For this purpose, a total of 36 pre-corroded specimens with pitting were tested against fatigue failure and monitored with Digital Image Correlation. In addition, the specimens were scanned with a high-resolution 3D scanner and converted to numerical models by reverse engineering, to determine the stress concentrations on the surface. In most cases the hotspots from the numerical model coincide with the crack location detected with Digital Image Correlation. The notch effect has a significant impact on the crack location and crack path.

1. Introduction

Support structures for offshore wind turbines (OWTs) are mainly made of steel and are highly susceptible to corrosion under maritime environmental conditions. Therefore, special requirements are set for the corrosion protection of OWTs [1,2]. Despite corrosion protection systems, corrosion cannot be completely avoided. Repairs of the corrosion protection system or even recoating of the support structures at sea are not feasible. For the technical assessment of further operation after (partial) failure of the corrosion protection system, the remaining service life under damaged corrosion protection must be determined reliably. Beside this, there is a growing interest in optimized design of support structures, due to the progressing use of the seas and associated cost increases. Both can be achieved by using more sophisticated fatigue strength concepts like the notch stress and the notch strain concept.

Corrosion causes thickness reduction due to uniform corrosion and local stress concentrations due to pitting. There is reliable knowledge about the thickness loss over time for different locations of the OWT [1,3], which are addressed in the standards as corrosion allowance [1,4]. The more crucial issue is pitting corrosion, were pits act like small notches and cause local stress concentrations [5–11]. This leads to fatigue life reduction, since the structures are exposed to high dynamic loads. Local stress concentrations can be considered in local [12–20], but so far, corrosion effects in local concepts are insufficiently defined.

In case of OWTs, different design standards [21–23] exist for fatigue issues. According to DNV, the fatigue design is predominantly carried out with the nominal stress concept, partly also with the structural stress concept [22]. There are different stress-life (SN) curves for the environmental condition Air, Cathodic Protection (CP) and Free Corrosion (FC). In the design of OWTs, a fully intact corrosion protection is assumed and therefore the SN-curves for Air are applied. From the point of time when there is no fully intact corrosion protection, the SN-curve for FC is used as a conservative approach for determining the (remaining) service life [24]. The SN-curves for CP and FC are derived from SN-curves for Air by reducing the SN-curves with the so-called Environment Reduction Factor (ERF) [25]. For the CP case, the design ERF is 2.5, while for the FC case ERF is equal to 3.0. These values are based just on a few tests performed on welded tubular joints and welded plates [25].

* Corresponding author.
E-mail address: shojai@stahl.uni-hannover.de (S. Shojai).

https://doi.org/10.1016/j.ijfatigue.2022.107128
Received 3 March 2022; Received in revised form 7 July 2022; Accepted 8 July 2022
Available online 12 July 2022

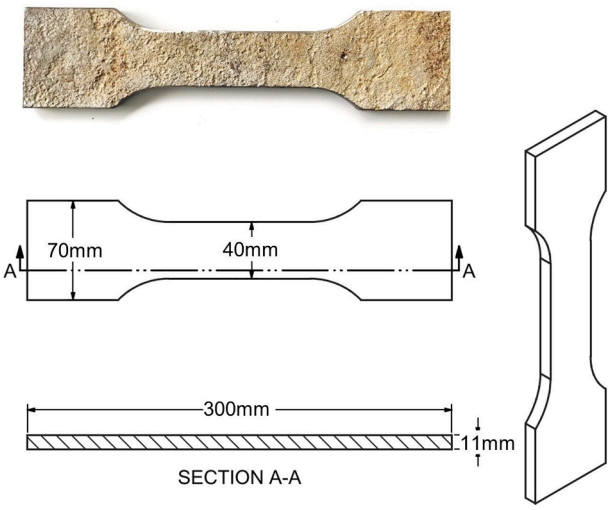

Fig. 1. Geometry of fatigue test specimen.

Table 1
Mechanical properties from tensile tests by Biglu [38].

	$R_{p0.2}$ [N/mm^2]	R_m [N/mm^2]	E-module [kN/mm^2]
Mean:	264.18	414.09	180.27
Deviation:	7.99	17.40	18.86
95%-quantile:	249.95	371.43	134.60
min:	246.66	356.00	107.34
max:	304.38	444.31	286.31

The welded tubular joints had an ERF < 3.0 in all tests, while the welded plates achieved values up to ERF $= 5.2$. Overall, ERF values between 0.8 and 5.2 were reported, indicating a high degree of scatter. This includes not only the scatter from the corrosive environment, but also the weld geometry, which is not documented. It is therefore assumed that the influence of corrosion on already heavily notched components (tubular joints) is smaller than the influence on weakly notched components (welded plates). A general reduction with a single ERF value, as carried out in the DNV standards, is then neither economical nor on the safe side. Hence, in the German BAW standard [26] a distinction between heavily and weakly notched components is made. Here, for FAT classes above FAT125, the FAT classes have to be reduced by two category levels in case of free corrosion, while no reduction is necessary for FAT classes below FAT56. Beside this, in the British standard BS 7608 [27] a reduction of the ERF depending on the relationship between the existing stress and the yield strength is considered. In case of welded specimen, where the local stresses are higher than in unwelded components, it leads to a reduction of the ERF values. A distinction between welded and unwelded specimens is indirectly possible here, while it is missing in DNV. However, a consideration of notch stresses with local concepts allows a distinction between strongly and mildly notched (corroded) components. Hence, in recently published research by Momber et. al. [28] a replica technique was developed, which enables the replication of the original topography of a corroded surface. This technique in combination with the findings of this paper, enables the evaluation of the remaining service life of corroded structures by using local concepts.

Nevertheless, the application of local concepts requires a detailed consideration of the impact of corrosion on the service life of structures.

Impact of corrosion: the service life of structures consists of the crack initiation and the crack propagation stage. Corrosion has an impact on the material in the crack initiation as well as in the crack propagation stage. Due to the acidic conditions under the rust layer, reported by Melchers et. al. [29], hydrogen can be produced and diffuse into the steel surface. According to Revie and Uhlig [30], and Marcus [31] the corrosion process includes an oxygen reaction and a hydrogen development process, in which hydrogen is released. The detailed chemical reaction process is illustrated in Li et. al. [32]. This leads to embrittlement of the material, which has an impact on the ultimate material strength as well as on both stages of the service life. Li et. al. [32] investigated the mechanical behaviour of low alloy mild steel G250 on specimen, which were exposed to different acidic conditions in an immersion test. With lower pH-values, the ultimate strength and the corresponding strain were reduced significantly. Mehmanparast et. al. [33] investigated that the crack propagation is two times higher in seawater then in air. Beside this, there is the already described impact on the surface geometry, which can accelerate the crack initiation stage due to high stress concentrations. This is of great importance, since the crack initiation time is supposed to be the leading life time in corroded specimens, according to recently published research of Qvale et. al. [34], where Digital Image Correlation (DIC) was used to identify crack initiations on a few corroded specimen extracted from offshore mooring chains. An overview of the current state of knowledge regarding the impact of corrosion on fatigue can be found in the review of Larrosa and Akid [8].

In this paper, the main focus is on the impact from the surface geometry on the fatigue performance. For this purpose, a total of 36 pre-corroded specimens are tested until fatigue failure occurs and monitored with DIC, in accordance with [34]. In addition, the specimens are scanned with a high-resolution 3D scanner and converted by reverse engineering to a numerical model that can be used to determine stress concentrations on the surface of the specimens. The stress concentrations are compared with the cracks recorded by DIC in order to make conclusions about the influence of the notch effect.

2. Test setup

2.1. Specimen

The specimens were cut out from pre-corroded approx. 11 mm transverse floor plates of a former bulk carrier. More information and first investigation on the surface geometry were carried out by Neumann [35] and Nugroho [36]. The exact exposure time to free corrosion environment and the environmental conditions are not recorded. The specimen geometry is shown in Fig. 1. The specimens were made by waterjet cutting. The edges were chamfered manually with $r = 1$ mm to avoid crack initiation on the sharp edges. The specimens were cleaned only with chemicals according to ASTM [37].

To determine the mechanical properties of the corroded steel, tensile tests were performed on 36 specimens by Biglu [38]. In Table 1 the results for ultimate tensile stress R_m, the yield stress $R_{p0.2}$ and the E-module are shown. The mean yield stress is 264 N/mm^2 while the 95%-quantile value is 250 N/mm^2. For the ultimate tensile stress, a mean value of 414 N/mm^2 and a 95 %quantile value of 371 N/mm^2 was conducted. Based on these tests a low alloy mild steel between S235 and S355 is assumed.

2.2. Fatigue tests and digital image correlation setup

The fatigue test setup is shown Fig. 2. The specimens were tested in a servo hydraulic testing machine, MFL HUS 60. The specimens were clamped at both ends. Some specimens were no longer straight after clamping at the upper end, which was due to the uneven surface at the clamping area. Clamping at the lower end straightened the specimen, resulting in out-of-plane moments. Since this is a constant moment, it can be interpreted as an additional mean stress, which has only a minor effect on fatigue. The testing frequency was 10 Hz. Up to 36 fatigue tests with $R = -0.1$, $R = 0.1$ and $R = 0.5$ were carried out. Most of the tests were conducted at $R = 0.1$, see Table 2. These results are used to obtain a S-N curve. Further test with $R = -0.1$ and $R = 0.5$ are carried out in order to investigate the impact of the mean stress.

Fig. 2. Fatigue test setup.

Table 2
Fatigue testing scope.

R = 0.1	R = −0.1	R = 0.5
22. tests	6 tests	8 tests

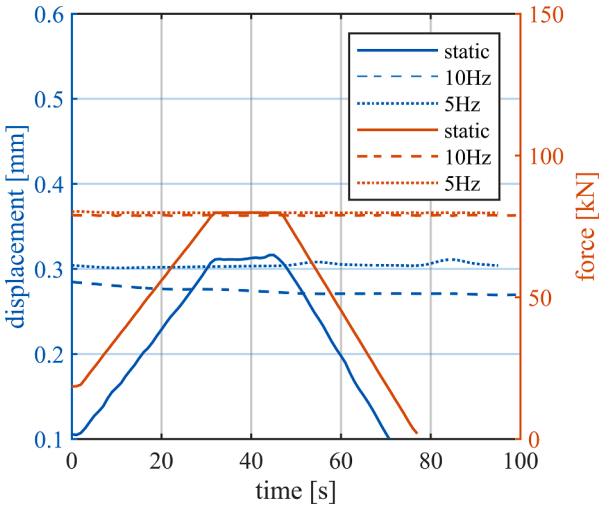

Fig. 3. Force-displacement diagram for static and dynamic test.

Additionally, the fatigue tests were monitored with digital image correlation (DIC) in order to determine the exact location of crack initiation as well as the exact fatigue life endurance in the crack initiation and crack propagation stage. This is necessary for the calculation with local concepts, where only the fatigue life endurance until crack initiation is considered.

2.3. Digital image correlation setup

The setup of the DIC system is shown in Fig. 2. It contains four high resolution cameras (sensors), two on each side, in order to capture the crack on both sides. In addition, it can capture strains and deformation in three dimensions. The sensor distance is set to approx. 520 mm, which allows to capture the specimens in a frame of approx. 120 × 90 mm. The smaller the sensor distance, the higher the resolution and the smaller the capturing frame will become. Hence, the setting here is a compromise between the resolution and capturing frame.

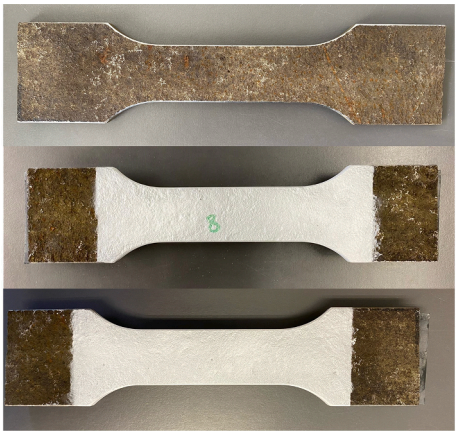

Fig. 4. Specimen preparation for DIC, white sprayed surface.

The usual application of a black and white pattern for DIC is not necessary here because of rugged surface. The rugged surface leads to shadows, which are used to correlate the images, and to lower reflections on the surface. Comparison shots have shown that the difference between specimen with pattern and without pattern is negligible. However, in this work a white spray paint was applied on the surface to light up the specimen surface (see Fig. 4). This allows to set a lower exposure time of the camera. A lower exposure time leads in turn to a lower delay between the trigger and the actual shot, which is an important issue in the application of DIC on fatigue test, where the loads alternate at high speed. However, the shadow correlation remains unaffected by the application of white spray paint. It should be mentioned that the pattern correlation can provide more accurate values for strain than the shadow correlation. For our application in this work, where the

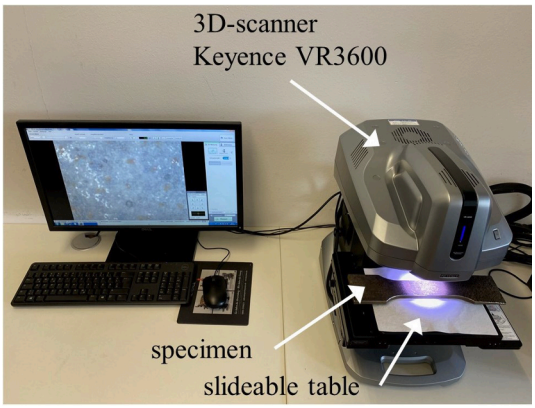

Fig. 5. 3D-scan with Keyence VR-3600.

cameras are relatively far away from the sample and the crack locations are of more interest than the exact strains, the shadow correlation is sufficient.

DIC calibration: Beside the mentioned delay due to the exposure time, there exist further delays between the testing machine signal and the DIC system. To ensure, that cracks are captured in every shot, the trigger has to be calibrated to the tensile load peak. Therefore, a static test has been run beforehand, in order to obtain the load–displacement relationship of a specific point on the specimen. In the second step, a dynamic test was run with 10 Hz (and also 5 Hz for further comparison) on the desired load level. Then, the displacement for the desired load level was compared. In Fig. 3 force and displacement over time are illustrated. The displacement for F = 80 kN is u = 0.31 mm in the static test, u = 0.30 mm at 5 Hz frequency and u = 0.27 mm at 10 Hz frequency. This corresponds to 96,7% (for 5 Hz) and 87% (for 10 Hz) of the load peak. To ensure a shot on the load peak, the trigger must be reduced respectively. Nevertheless, cracks are visible in both cases. This is also reported in [39].

For the fatigue tests, the trigger was set to approx. 85% of the load peak. Depending on the load level, at every 1000 or 2000 load cycle a shot was taken.

2.4. Crack detection using DIC

With the application of DIC it is possible to capture the strains as well as the crack initiation and the crack propagation over the testing period. All 36 specimens were investigated with DIC. For all specimens the fatigue life until crack initiation was obtained by going manually through the DIC shot series, until the cracks became visible. Two values were documented in this way, the fatigue lifetime N_{C1} and N_{C2}.

The definition of N_{C2} is based on Radaj in [12] and Radaj and Vormwald [40], where the technical crack is defined as a crack between 0.5 and 2 mm length and 0.5 mm depth, see also Braun et al. [41]. This definition also corresponds to the definition in the background documentation of Eurocode 3 [42], where the technical crack is defined as the first crack either detected visually or by measuring the deformation behaviour. However, there are several methods to determine the technical crack using DIC. According to Friedrich and Ehlers [39,43], the technical crack is reached at a strain of>1% over a length of 2 mm. Hutt and Cawley [44] and Schürmann [45] defined the crack by the displacement in axial direction. Schürmann used the strain to detect the crack location and the displacement to detect the number of load cycles to crack initiation. This is possible since a displacement gap occurs in the area of the crack, whereby a gap of approx. 0.004 mm was chosen as an indicator. Alternatively, Qvale et. al. [34] defined the macroscopic crack at an inter-node displacement of 0.002 mm. In the investigations carried out here, the approach according to Friedrich and Ehlers was chosen for the detection of the technical crack. Hence, N_{c2} is defined at a crack that has a strain of at least 1% over a length of about 2 mm. This criterion is in line with the definition according to the Eurocode, since the cracks are also visually detectable. Since the cameras of the DIC system can also detect cracks smaller than 2 mm, in addition to N_{c2}, the first visible crack at N_{C1} was documented. Hence, N_{C1} is defined at a crack of at least 1%, but with a length of smaller than 2 mm.

It should be mentioned that higher DIC resolutions enable more accurate data on the displacement and strain during the fatigue test and thus could lead to a different ratio of crack initiation and crack propagation lifetime.

2.5. 3D-scanning of specimen and reverse engineering method

3D-scanning: Before the fatigue test, the specimens were scanned with a high-resolution 3D measuring system Keyence VR-3600 (Fig. 5).

The scan and the assembling into a 3D-model requires several steps shown in Fig. 7. The procedure starts with scanning the surface from all sides separately (see Fig. 6) and exporting as STL-files. In the next step, the lateral surfaces are trimmed and all surface scans are pre-positioned in order to avoid complications in the assembling procedure. Hereafter, the surface scans are merged one after the other, with the best-fit command within the GOM Correlate software. The application of the best-fit command requires the existence of an common area in each scan. This is ensured with the chamfered edges, which are captured from the upper and the lower as well as from the lateral scans. Beside this, the lateral scans ensure the exact caption of the specimen thickness. It should be noted that the quality of the scan depends on the grid size. Lower grid sizes lead to high amount of data and are very demanding to handle. However, in this research the scans were conducted with a grid size up to 0.02 mm.

Reverse Engineering: The reverse engineering method is used to create a solid model from the assembled 3D-model available in STL format. The transformation to a solid model is required due to following aspects:

The curvature of the surface in STL format is not continuous, because it consists of a series of individual facets that are connected to each other, see Fig. 8 b). This would lead to singularities in the subsequent numerical analysis.

The faceted surfaces require too large amounts of data for illustration (high number of points, lines and facets).

The procedure of obtaining a solid model from STL-format is described in Shojai et. al. [46]. For this purpose, so called Non-Uniform Rational B-Spline (NURBS) surfaces are used. NURBS surfaces are described by two-dimensional, mathematically defined polynomial functions of higher order, which fit the shape of the faceted geometry. The advantage of NURBS surfaces are, that they need much less data for the description of the surface and have a continuous curvature. The quality of the fit depends on the number of polynomial functions per area. In the reverse engineering software Ansys SpaceClaim, this can be controlled through the number of the grids per area (grid rate), see Shojai et al. [46]. Higher grid rates lead to better fitting of the facets and are thus more accurate. In [46] a grid rate of R = 3 [1/mm] (120 grids per 40 mm length) was sufficient. Here a grid rate of R = 7–8 [1/mm] (120 grids per 15 mm length) was determined as sufficient. The difference is caused by the scan quality, which is higher with the VR-3600

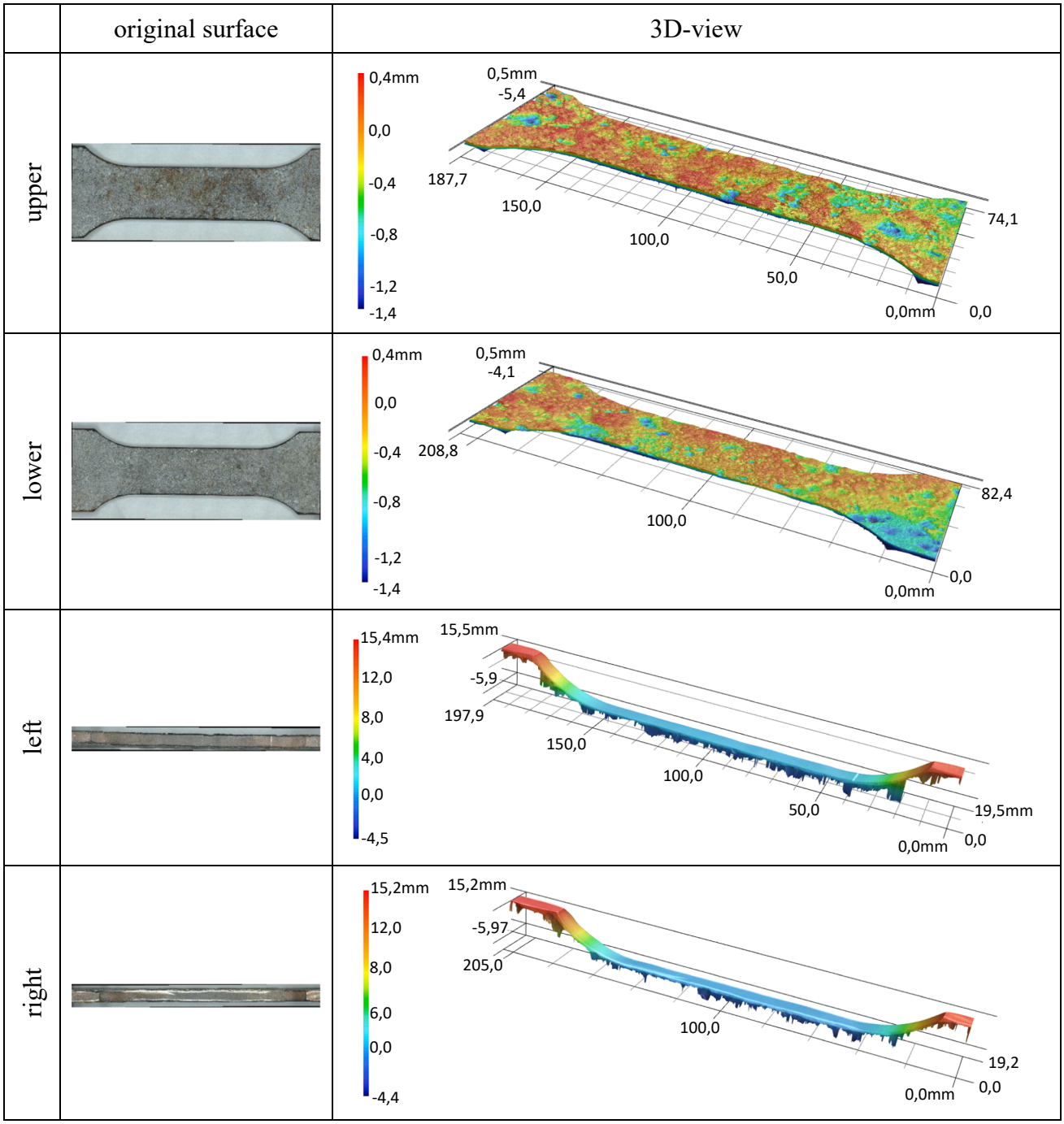

Fig. 6. High resolution shots of a corroded sample from all sides.

scanner (0.1 mm grid size in the 3D-scan). A scan with smaller grid size with higher scan quality, requires high grid rates for fitting the faceted surface. The impact of different scan qualities in the assessment of fatigue strength is an object of ongoing research and is not discussed here. However, it is not possible to create a solid model by transferring the entire surface in single NURBS surface. Hence, the surface is split into so-called NURBS-patches [7 17] and merged into a solid model afterwards, see Fig. 8 right. Up to 80 patches were required to assemble a solid model according to Fig. 8.

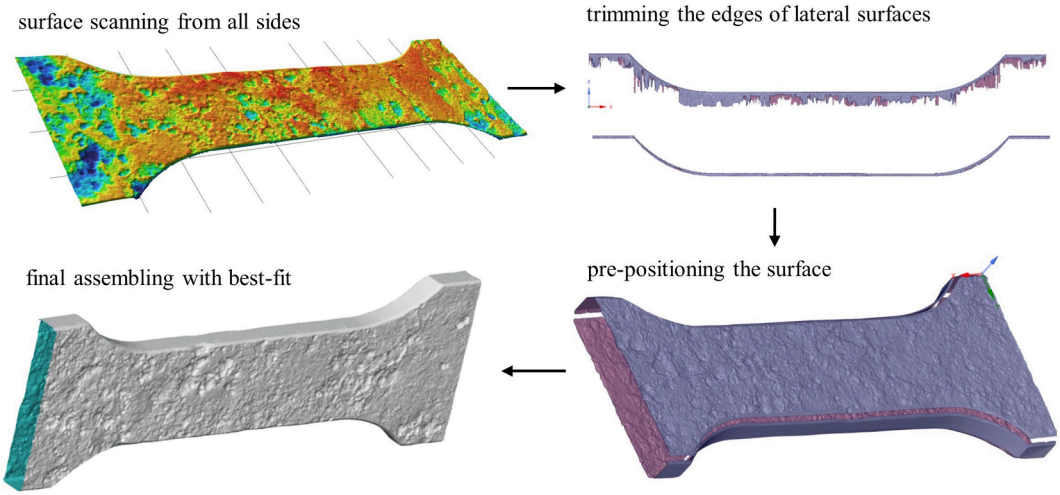

Fig. 7. Assembling the scans into a 3D-model as STL-data.

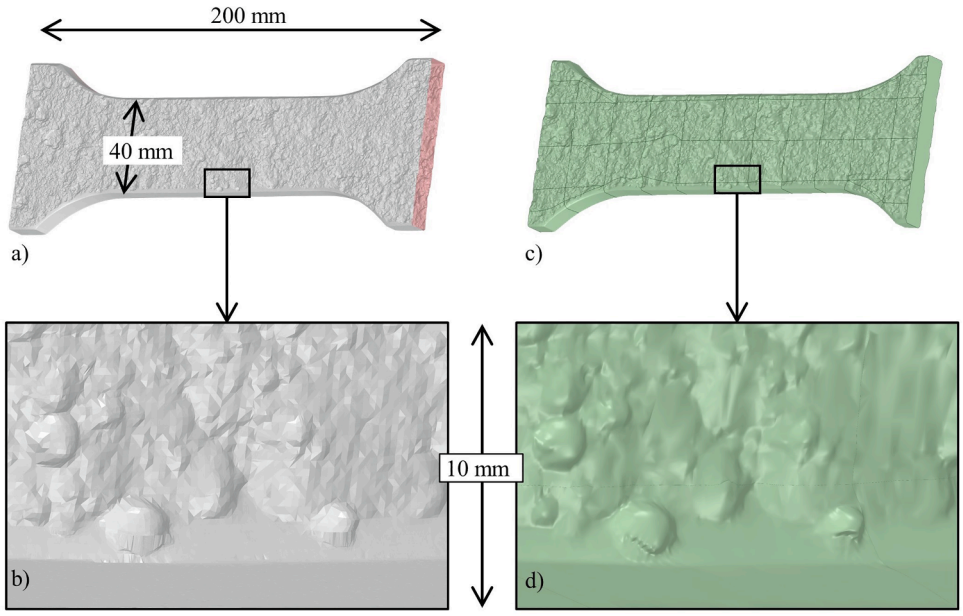

Fig. 8. Faceted 3D-model in STL-format with non-continuous surface in a) and b). Solid model with NURBS-patches with continuous surface in c) and d) - both for specimen P.01.

3. Numerical analysis

3.1. Numerical model

The numerical model with the boundary conditions for the analysis of the stress concentrations are shown in Fig. 9 b). If the applied force is adjusted to the cross section, the stress results on the surface are equivalent to the stress concentrations. Since the cross section varies along the specimen, the cross-section area is determined by the mean of 5 different locations at an interval of approx. 20 mm in the region of the tapered area of the specimen. An example of the cross section is given in Fig. 9 a). For the meshing quadratic tetrahedral elements were used in order to fit in the rugged surface and achieve a fast convergence. Studies on the element size have shown, that an element size of 0.3–0.4 mm is required [46] to ensure, that the maximum stress concentration location doesn't change. After the maximum stress concentration location has been ensured, a convergence study only for that area has been conducted. This reduced the number of elements and computing time significantly. The initial element size is shown in Fig. 9 c).

3.2. Convergence study

The convergence study has been carried out in the area of the maximum stress concentration (see Fig. 9 e). For this purpose, the adaptive convergence tool in Ansys Workbench has been used. The final mesh and the updated stress concentrations are shown Fig. 10 on the left

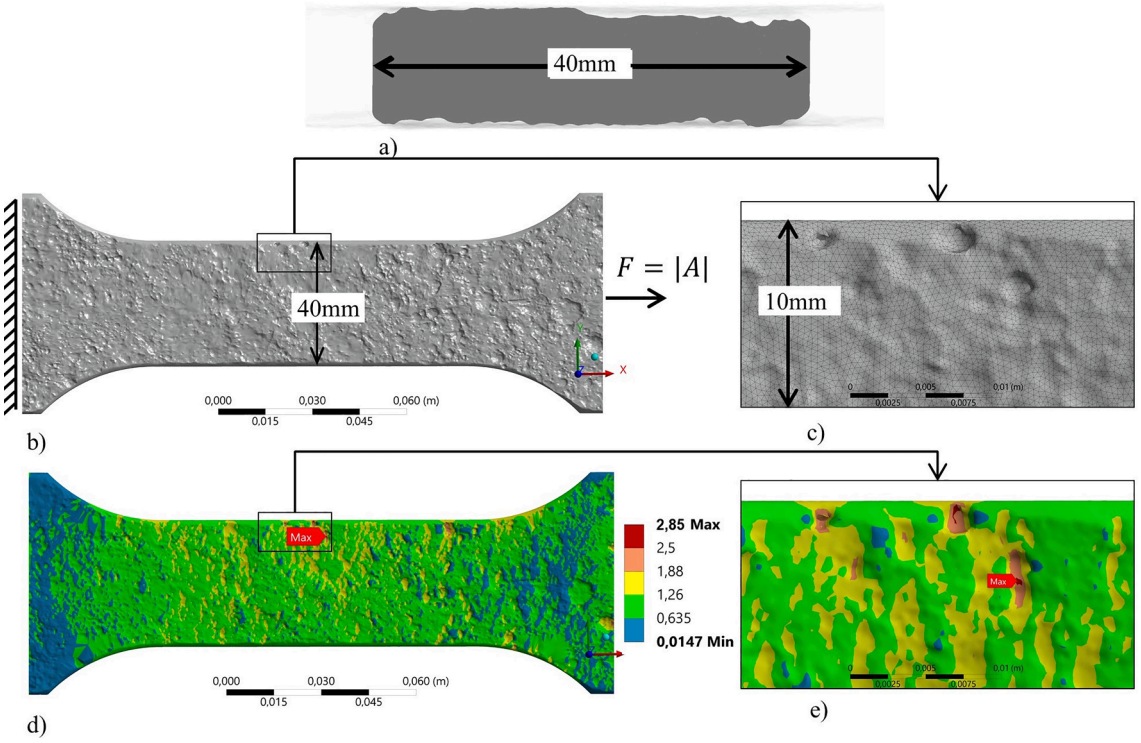

Fig. 9. Specimen P.01 a) cross section A at maximum stress concentration, b) solid 3D-model, c) initial surface mesh of solid model, d) results of numerical simulation, e) maximum stress concentration before convergence study.

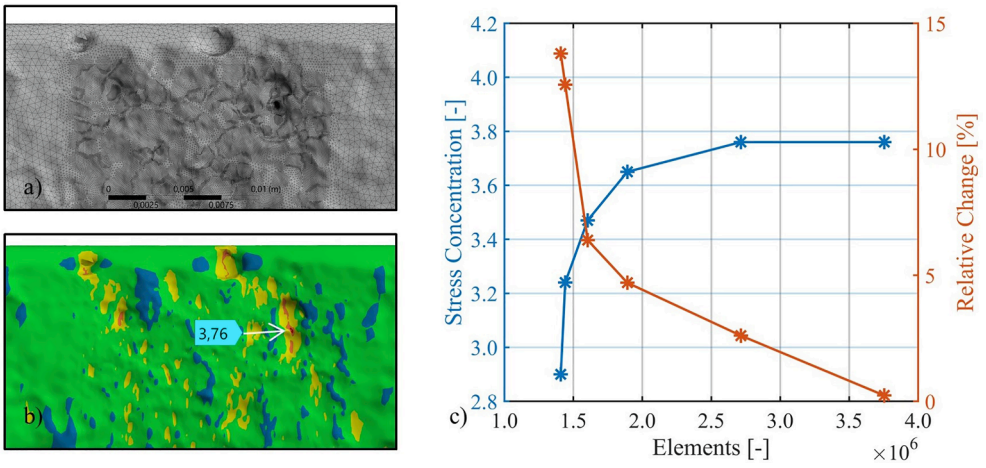

Fig. 10. Specimen P.01, adaptive convergence study applied on in the area of maximum stress concentrations. a) refined surface mesh at last stage, b) converged stress concentration c) convergence plot.

(a and b). The element size in the stress peak is 0.01 mm. Around the stress peak the element size is 0.05 to 0.1 mm. The change in the stress concentration due to refinement is not only caused by the FEM-dependent approximation of the real solution, but also on the rugged surface of the corroded specimen. The fine mesh shown in Fig. 10 b) fits better into the surface of the solid model than the initial mesh shown in Fig. 9 c). Finer meshes lead to more accurate description of the rugged surface and lead to higher stress concentrations. This is also shown in Fig. 11, where an element size of 1.0 mm (Fig. 11, b) obviously can describe the rugged surface better than an element size of 1.8 mm (Fig. 11, c). This leads to the fact, that the surface geometry changes in every refinement step, which in return leads to higher initial slopes in the convergence study, see Fig. 10 c). This behaviour is intensified by finer NURBS surfaces and can lead to very high stress concentrations.

However, for plausible results, a harmonization between the scanning grid size, the NURBS grid rate and the element size of in the numerical simulation is indispensable. In the case of the specimen shown in Fig. 10, the stress concentrations converged to $\alpha_k = 3.76$ from the initial value of $\alpha_k = 2.85$ (see Fig. 9) and can hence interpreted as a plausible result. All specimens were investigated in this manner. The results are presented in chapter 4.

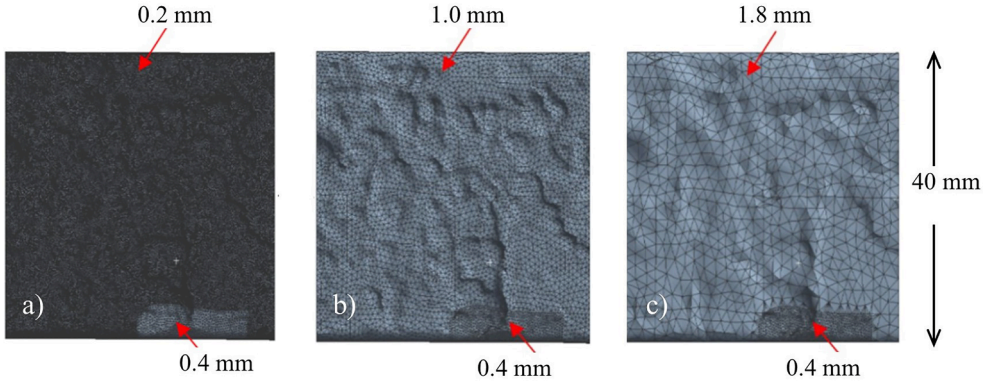

Fig. 11. Impact of mesh element size on surface description for 0.2 mm (a), 1.0 mm (b) and 1.8 mm (c).

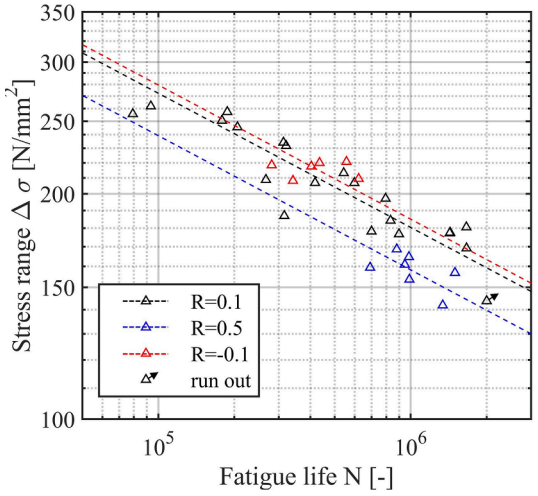

Fig. 12. Fatigue test results for different R-ratios and corresponding 50%-quantile S-N curves.

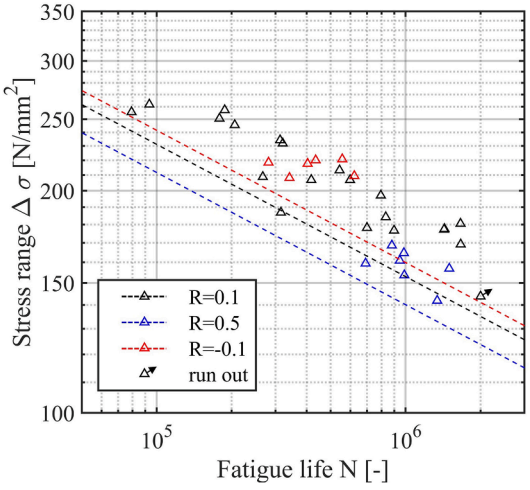

Fig. 13. Fatigue test results for different R-ratios and corresponding 97.7%-quantile S-N curves.

Table 3
S-N curve parameters.

		50%		95%		97,7%	
m_1	R	$\Delta\sigma_C$ (FAT)	log a	$\Delta\sigma_C$ (FAT)	log a	$\Delta\sigma_C$ (FAT)	log a
5.58	−0.1	163.4	18.651	146.1	18.380	141.2	18.297
	0.1	159.3	18.590	139.3	18.264	135.1	18.191
	0.5	139.8	18.273	127.2	18.045	123.8	17.978

4. Results and discussion

4.1. Fatigue tests results

The fatigue test results with corresponding load values, load ratios, cross section areas and stress ranges for the specimens are summarized in Appendix A, Table 5. The cross-section area A_{ave} is determined according to chapter 3.1 with the mean of 5 different locations in the tailed area of the specimen. The results are statistically evaluated to obtain the SN-curve for the high cycle fatigue (HCF) region, which is defined between $N = 10^4$ and $N = 7x10^6$ in Eurocode 3 [21], DNV [22] and IIW [14]. The SN-curve is defined as.

$$N = 2\cdot10^6\cdot\left(\frac{\Delta\sigma_C}{\Delta\sigma}\right)^{m_1} \quad (1)$$

where N is the number of cycles to failure, Δσc is the characteristic stress range at $N = 2x10^6$, Δσ is the stress range used as variable and m_1 is the slope in the HCF region. Equation (1) can be transformed into the log scale and is then stated as a linear equation according to Basquin [47]:

$$logN = loga - m_1 \bullet log\Delta\sigma \quad (2)$$

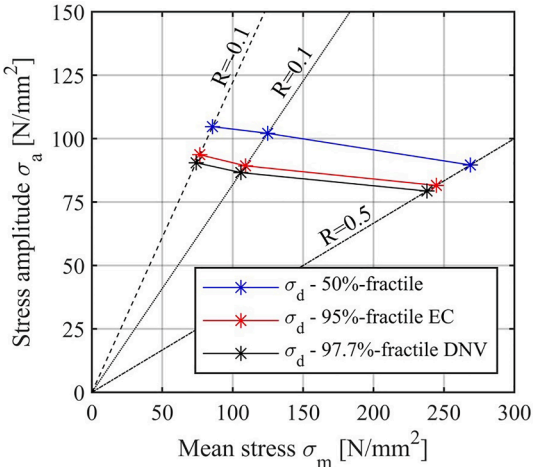

Fig. 14. Haigh-diagram for fatigue life endurance $N = 5x10^5$.

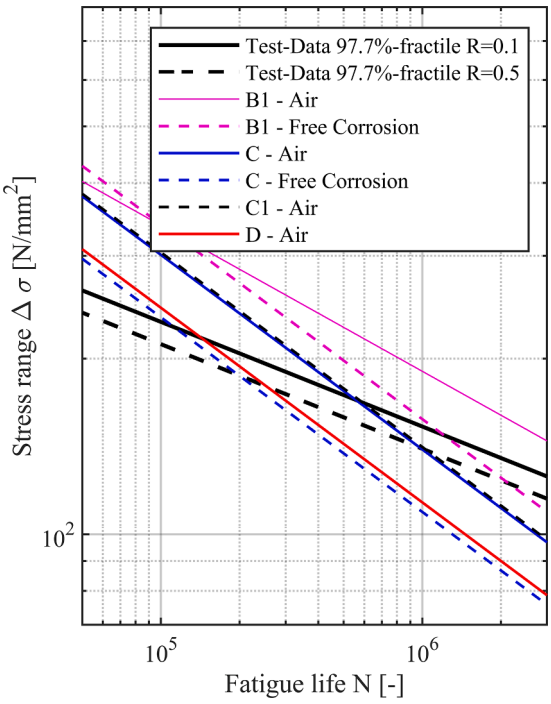

Fig. 15. Comparison of test data to design S-N curves from DNV.

in accordance to:

$$y = b - m \bullet x \tag{3}$$

Here, log a in equation (2) defines the axis intercept similar to b in equation (3) and is then used to calculate the characteristic stress range $\Delta\sigma_C$.

For the evaluation of the parameters log a and m_1 the pearl-string method according [48] is used. Therefore, a linear regression using the least squares method in the direction of the number of cycles is applied in the first step. In the second step, the statistical evaluation is carried out. For this purpose, all test results are projected onto an arbitrary load horizon on which the log a value for the survival probabilities are calculated. This procedure allows the evaluation of test data with varying stress ranges, as listed in Table 5. It should be noted, that there are varying stress ranges, even though the applied loads are the same. This is caused by different cross section areas for each specimen (see Table 5, column 2 and 6) and rules out the application of the horizon-method.

The fatigue test results with the corresponding 50%-fractile curve are plotted in a S-N diagram in Fig. 12. The slope m_1 was determined based on the fatigue tests conducted with R = 0.1. For the curves of R = −0.1 and R = 0.5 the same slope is assumed, since there are not enough data to determine a slope reliably. The corresponding parameters for log a and $\Delta\sigma_C$ are listed in Table 3. For R = −0.1 and R = 0.1 there is only little difference in the fatigue resistance, as illustrated in Fig. 12. It should be noted, that due to the small difference and the small number of specimens, no clear statement about the influence of the mean stress can be made, when comparing R = −0.1 and R = 0.1 results. However, compared to R = 0.5 the test results for R = 0.1 show clearly higher fatigue resistance. This is also illustrated in the Haigh-diagram shown in Fig. 14, where the stress amplitudes and the corresponding mean stresses for the number of cycles of N = $5x10^5$ are plotted for different confidence levels. The number of cycles of N = $5x10^5$ selected for the Haigh-diagram evaluation is close to the test results for R = −0.1 and R = 0.5. This ensures that the effect from the assumption of equal slopes for all mean stress ratios is minimized. It becomes evident, that with

Table 4
Detail categories according to DNV.

Constructional detail	Detail category	Environmental condition	Slope m_1	Slope m_2	log a_1	log a_2	$\Delta\sigma_c$ (FAT)
Rolled plates and flats	B1	Air	4	5	15.117	17.146	160.0
Rolled plates and flats	B1	FC	3	5	12.436	12.436	110.9
Rolled plates and flats + pitting corrosion	C	Air	3	5	12.592	16.081	125.0
Rolled plates and flats + pitting corrosion	C	FC	3	3	12.115	12.115	86.7
Butt welds + ground flush to plate surface	C1	Air	3	5	12.449	16.081	112.0
Butt welds + convexity smaller than 10% of weld width	D	Air	3	5	12.164	15.606	90.0
Test data – R = 0.1	C	Air	5.58		18.191		135.1
Test data – R = 0.5	C	Air	5.58		17.978		123.8

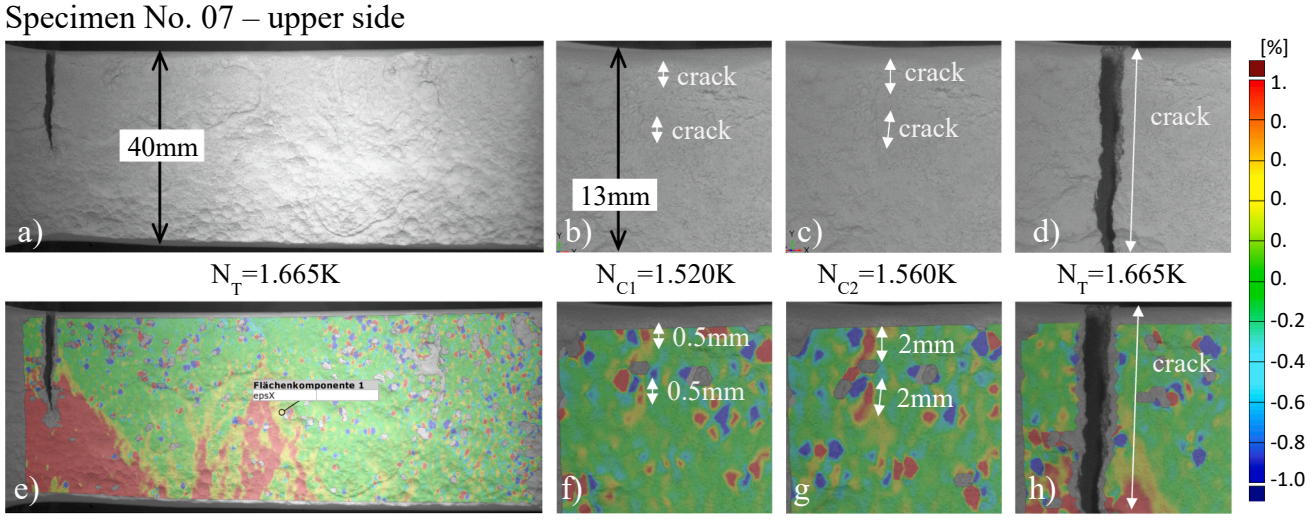

Fig. 16. DIC plot for crack initiation, crack propagation and fracture of Spec. No. 07.

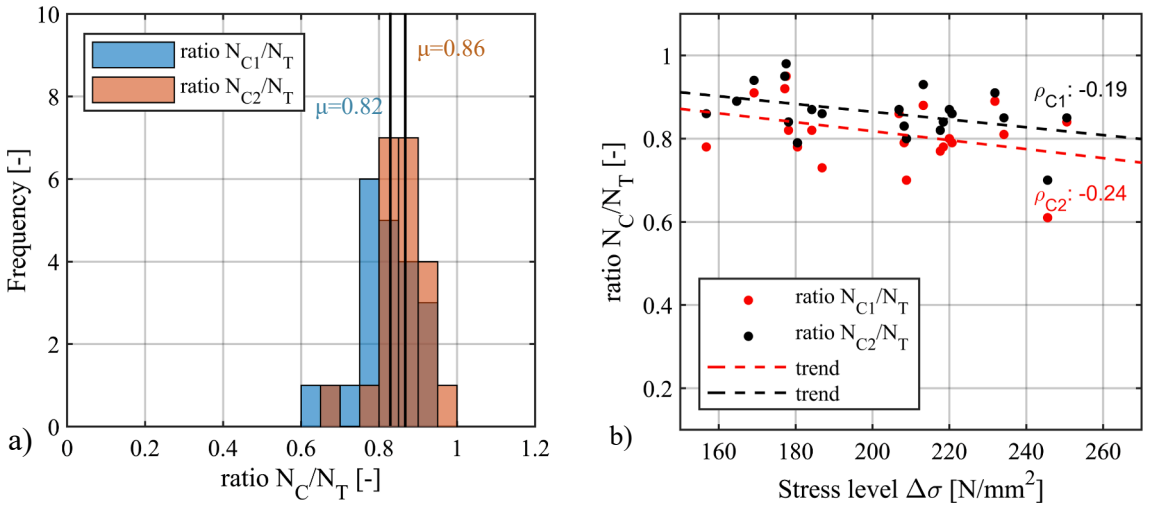

Fig. 17. Frequency plot for the ratio of cycles until crack initiation to total cycles (a) and relationship between crack initiation ratio and the corresponding stress level (b).

higher mean stresses, the stress amplitude for reaching N = 5x10^5 is getting smaller. This is in accordance to Eurocode 3 and DNV [15,16], where the stress range can be reduced up to 60% for mean stresses below R = 0. For stress ratios above R = 0, there are no distinctions made in Eurocode 3 and DNV. In the IIW recommendations [15] the reduction already starts at R = 0.5 and corresponds better to the test results in the range of R > 0. Nevertheless, for the purpose of further comparisons the conducted 97.7%-fractile S-N curves for R = 0.1 and R = 0.5 are used (see Fig. 13).

Comparison with DNV rules: In Fig. 15, the conducted S-N curve for R = 0.1 and R = 0.5 with 97.7% probability of survival is plotted alongside of S-N curves for different detail categories according to DNV. The corresponding constructional details, environment conditions, slopes with log a values and the stress range Δσc for the plotted curves are listed in Table 4.

According to DNV rolled and extruded plates corresponds to details category B1. In case of additional stress concentrations due to pitting corrosion on the plate surface, the use of curve C is recommended. Curves C1 and D are required for transversal butt welds. The slope of the conducted fatigue test with $m_1 = 5.58$ is higher in all cases compared to the DNV curves. This leads to a flatter S-N curve and greater values of the stress range $\Delta\sigma_C$ compared to all curves listed in Table 4, beside curve B1-Air. It is worth mentioning, that the test data with $\Delta\sigma_C = 135.1$ N/mm^2 and $\Delta\sigma_C = 123.8$ N/mm^2 (for R = 0.1 and R = 0.5 N/mm^2) indicates higher stress ranges at N = 2x10^6 than curve C1-Air and D-Air with $\Delta\sigma_C = 112$ N/mm^2 and $\Delta\sigma_C = 90$ N/mm^2. This is a valuable finding, since it allows the implicit comparison of the pre-existing notch effects of butt welds to the notch effect of corroded base material.

4.2. Digital image correlation results

As mentioned, DIC was used to track strain and displacement as well as crack initiation. DIC was applied on all 36 specimens. In 21 cases, the crack was inside the DIC frame. The determination of the crack initiation locations and the definition of the technical crack are described in chapter 2.4.Two values were documented accordingly, the fatigue lifetime N_{C1} and N_{C2}. The measured crack lengths for N_{C1} and the related fatigue lifetime is documented in Table 6 (Appendix B).

In Fig. 16 the DIC shots (plot a) to d)) and the corresponding strains in [%] (plot e) to h)) are shown exemplary for specimen No. 07 at different number of cyclys N_{C1}, N_{C2} and N_T. The length of the first visible crack at N_{C1} is directly measured at the DIC shot (plot b)). The crack length at N_{C1} is smaller than 1 mm and is only slightly visible in the strain plot, while it becomes clearer at N_{C2}. From N_{C2} the crack grows until fracture N_T (total fatigue life). It has to be noted, that dark blue and dark red colour in the strain plots are signal noise, which are also enhanced due to the very rugged surface, and hence can be ignored.

Moreover, the crack initiation ratios for N_{C1} and N_{C2} to the total fatigue life N_T were determined for all tests, where the crack was inside the DIC frame (see Table 6 (Appendix B)). The results are plotted in a frequency plot in Fig. 17 (a). The mean ratio of $r_{C1} = N_{C1}/N_T$ is $\mu = 0.82$, while the standard deviation is $\sigma = 0.06$. The mean ratio of $r_{C2} = N_{C2}/N_T$ with $\mu = 0.86$ is slightly higher with a smaller deviation of $\sigma = 0.04$. It can be concluded, that the crack initiation stage predominates the fatigue life of the tested specimens. This behaviour can be explained by the small thickness of the specimens and thus small capacity for crack propagation and the low notch acuity [41,49–51].

The mean difference between N_{C1} and N_{C2} is $\mu_{(1-2)} = 0.05$, see Table 6. It means that on average 5% of the total lifetime is needed to reach a crack length of 2 mm, after the first visible crack initiation. It has to be noted, that the documentation of the first visible crack is highly dependent on the evaluator, because there is more room for interpretation, while it is clearly defined, when a crack length is given. Hence, for upcoming publication, which will deal with the evaluation of the fatigue resistance based on the notch strain concept and the subsequent comparison of the determined fatigue life, the fatigue life corresponding to an Initial crack length of 2 mm crack will be used as reference. In addition, the correlation between the load stress level and the crack initiation time, expressed by the ratio $r_c = N_C/N_T$, is investigated. According to [40] and [52] for welded components there is a dependency between stress level and crack initiation and crack propagation lifetime, where low stress levels lead to higher lifetime in the crack initiation stage while high stresses lead to higher lifetime at the crack propagation stage. For this reason, in Fig. 17 (b) the crack initiation ratio is plotted over the corresponding stress level. It can be concluded, that for all specimens, which were inside the DIC frame (see Table 6 in Appendix B), there is only little correlation between the stress levels and the ratio. This is indicated by the trend line plotted Fig. 17 (b) and the corresponding correlation values of $\rho_{C1} = 0.19$ and $\rho_{C2} = 0.24$. This is assumed to be due to the fact that the nominal stress illustrated here does not reflect the local situation at the notch.

4.3. Numerical analysis results

The numerical analysis were carried out for all specimen listed in Table 6, according chapter 3. For each specimen, the crack location, the maximum resulting local notch stress as well as the notch stress at crack location were documented. Moreover, the coincidence of the

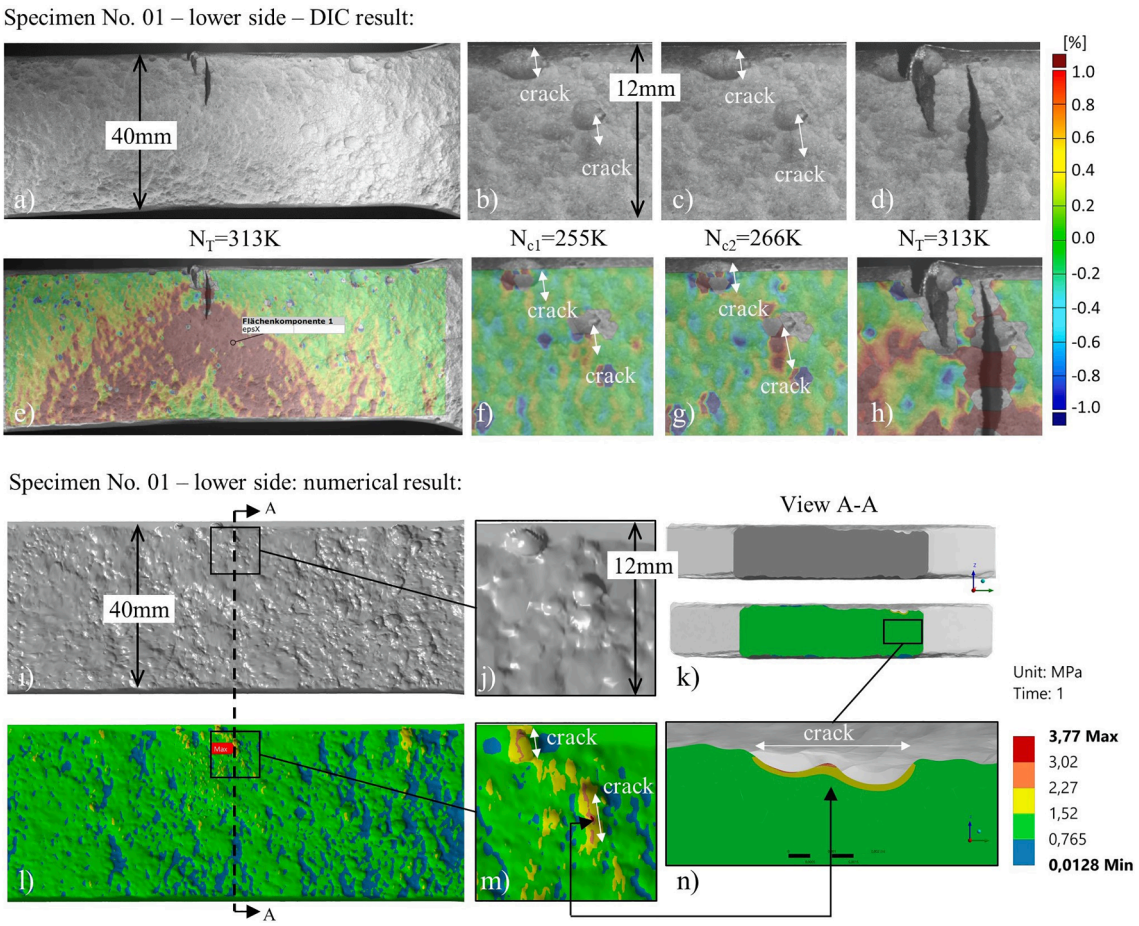

Fig. 18. Comparison of DIC results with numerical determined stress concentration results for specimen No. 01 – coincidence level 1.

numerically determined hotspot stress with the actual crack location was documented. For this purpose, three levels of conformity are introduced:

- Level 1: The max. stress concentration coincides with actual crack location and the crack path. The ratio between stress concentration at the crack location and the max. stress concentration is 1.0.
- Level 2: The 2nd max. stress concentration coincides with actual crack location and the crack path. The ratio between stress concentration at the crack location and the max. stress concentration is higher than 0.8.
- Level 3: The 2nd, 3rd or 4th max. stress concentration coincides with actual crack location and the crack path. The ratio between stress concentration at the crack location and the max. stress concentration is lower than 0.8.

The coincidence of the hotspots was investigated through the comparison of the DIC-shots with the numerical analyses results. For specimens, where the cracks occurred outside the DIC frame, the crack location was determined by inspection of the beach marks.

In Fig. 18 the DIC results and the numerical simulation results are illustrated. As described in section 2.3, the DIC shots were taken from both sides (upper side and lower side). Here, only the side, at which the first crack initiated, is documented. For specimen No. 01 (Fig. 18) the crack occurred at the lower side. The crack initiation as well as the propagation are shown in the DIC shots and in the corresponding strain plots (Fig. 18 a) to h)). In Fig. 18 i) to n) the obtained stress concentrations from the numerical analysis are shown for the same locations. From the comparison of plot f) with m) it becomes evident, that the max. stress concentration is in accordance to the crack initiation location. Moreover, the crack propagation follows fully the stress concentration path, which is an indication of the high impact of stress concentrations on the fatigue life. On plot k) and n) the cross section of the numerical model and the corresponding stress distribution is plotted. It shows, that the max. stress concentration is at the intersection of two overlapping pits. This is in line with Shojai et. al. [7], where a double pit model was introduced for the calculation of stress concentrations factors and the approach whit a single pit model has been questioned. However, the numerical results of specimen No. 01 fully matches with the results of the fatigue test and is hence categorized in the coincidence level 1.

In Fig. 19, the result of specimen No. 05 is shown as an example of the coincidence level. The max. stress concentration from the numerical analysis is $\alpha_{k,mx} = 3.51$, but it doesn't match with the crack location shown in plot a) to h). The actual crack is located inside the black frame (see Fig. 19, l) and m)), where the local max. stress concentration is $\alpha_{k,crack} = 3.25$. This is the second highest local value of the stress

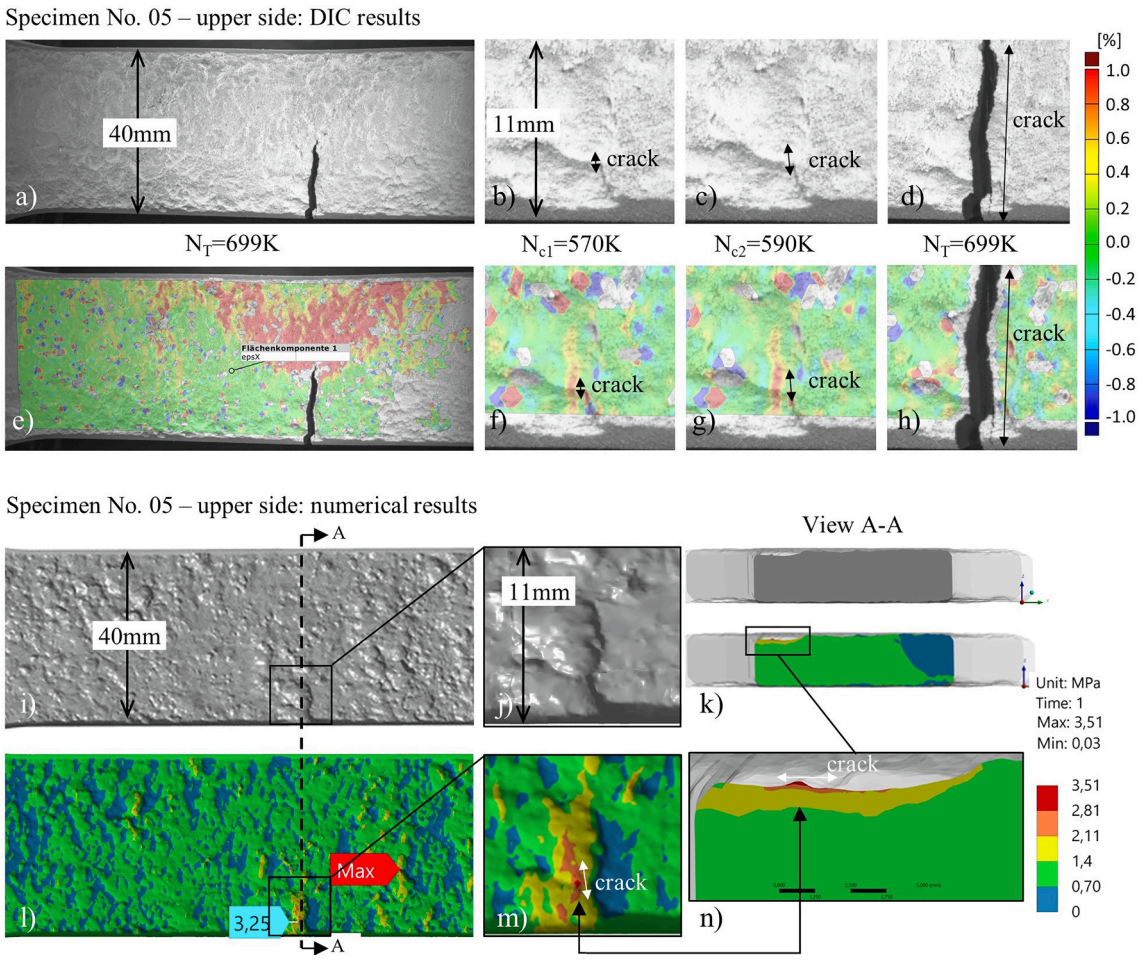

Fig. 19. Comparison of DIC results with numerical determined stress concentration result for specimen No. 05 – coincidence level 2.

concentration and is only marginally lower than the absolute max. stress concentration. The ratio defined as $r_\alpha = \frac{\alpha_{k,crack}}{\alpha_{k,max}}$ is $r_\alpha = 0.93$. Nevertheless, the crack path fully agrees with the stress concentration, when plot f) and m) are compared. Besides this, the crack initiated here again at the intersection of two overlapping pits as shown in plot k) and n).

In the coincidence level 3 the same pattern as in level 2 can be observed. The difference is only in the ratio r_α, which is defined as lower than 0.80 in level 3.

However, in Fig. 20 the crack initiation locations for all specimen (with cracks inside the DIC frame) at coincidence level 1 and the corresponding numerical results for the stress concentrations are shown. The max. stress concentration location is labeled with a red banner and matches with crack location. It follows, that for 13 out of 21 specimens the first crack initiated at the max. stress concentration location.

In Fig. 21 the specimens of coincidence level 2 and 3 are plotted. The red banners show the max. stress concentrations location, while the blue banners indicate the crack location and the corresponding stress concentration. Only 8 of 21 specimens belong to that level.

The max. stress concentrations and the stress concentration at the crack location are plotted in Fig. 22 for all specimens. The related data are provided in Appendix C, Table 7. The values for both are, besides specimen No.15 and No.33 with $\alpha_k > 5.0$, at a comparable level. This can be also observed in the frequency plot of the max. stress concentrations in Fig. 23. The mean value for the max. stress concentrations is $\mu = 3.55$ and for the stress concentrations at the actual crack location $\mu = 3.30$. The corresponding standard deviations are respectively $\sigma = 0.56$ and $\sigma = 0.61$, which indicates a small scatter. Beside this, it becomes evident from Fig. 22, that the difference between the max. stress concentration and the stress concentration at the crack is comparably small as well. This can be also observed in Fig. 24, where the ratio rα are illustrated in a frequency plot. Only a few specimens have a ratio smaller than $r_\alpha = 0.8$. For 31 of 34 specimens, the ratio is higher than $r_\alpha = 0.8$. It should be noted, that in Fig. 22, Fig. 23 and Fig. 24 all of the 34 specimens were considered in the evaluation, even though the crack was outside the DIC frame.

It is assumed that the difference between the predicted and the actual crack location is caused by various local structural support mechanism like micro and macro structural support. The here evaluated notch stress concentration is only depending on the geometry of the real corroded specimen and does not consider local plastification, although crack initiation is controlled by local strain [53,54]. Those plastification lead to lower fatigue-effective stresses, especially in mild steel. There are several methods in order to consider this effect like the stress gradient approach, the stress averaging approach [12,13], the theory of critical distances of Taylor [55] or the widespread approach of Neuber with an

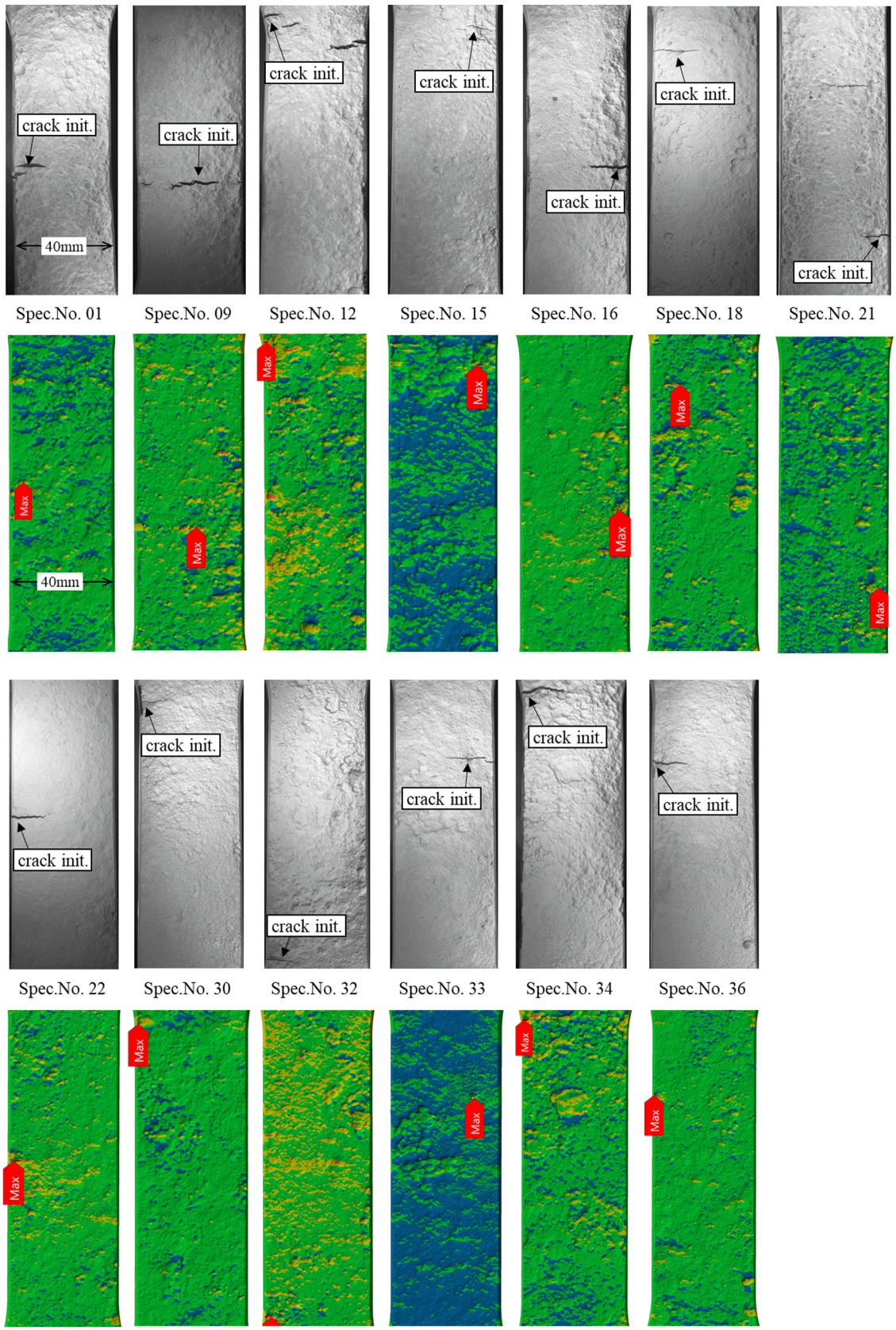

Fig. 20. Specimens of coincidence level 1 with corresponding crack location and max. stress concentrations location (red banner). (For interpretation of the references to colour in this figure legend, the reader is referred to the web version of this article.)

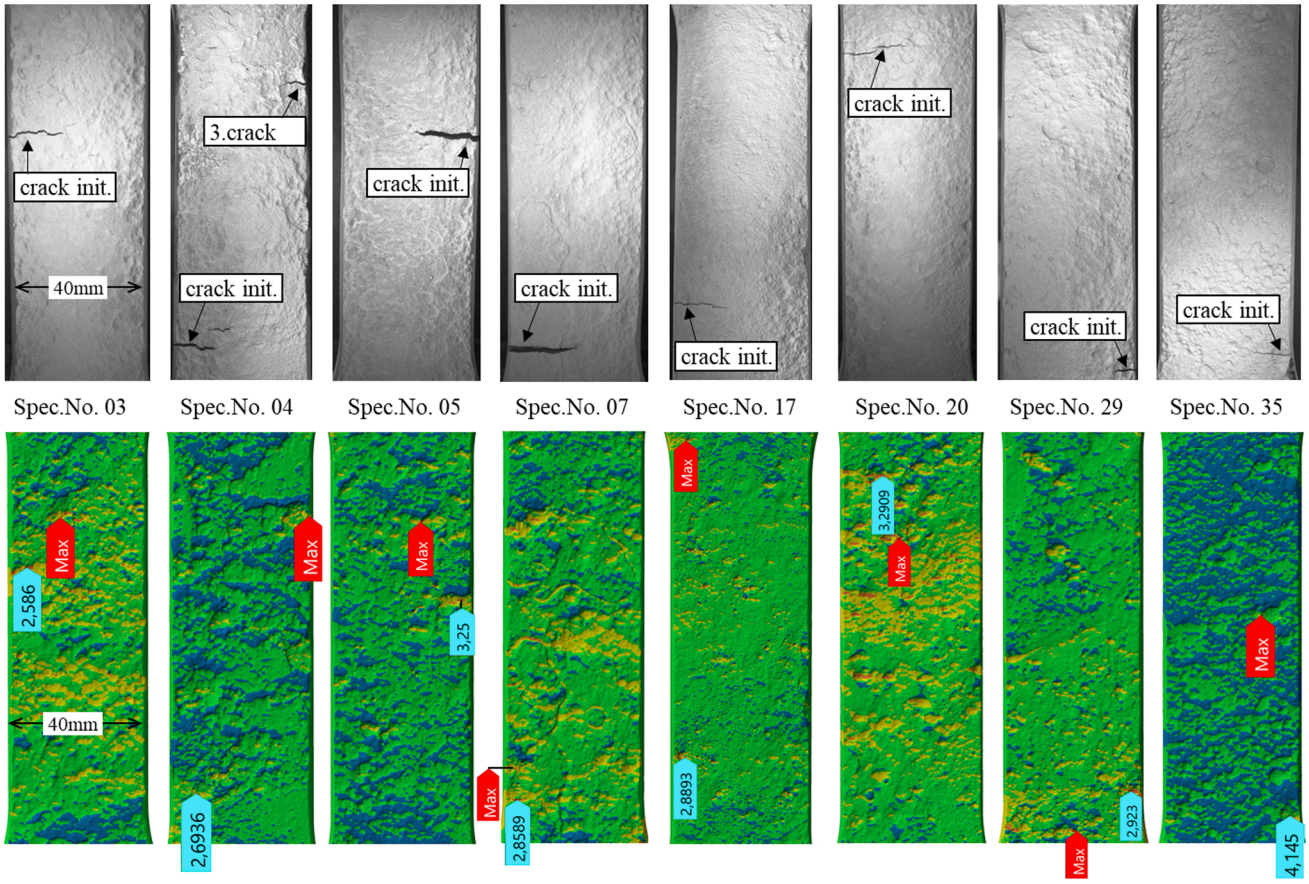

Fig. 21. Specimens of coincidence level 2 with corresponding crack location (blue banner) and max. stress concentrations location (red banner). (For interpretation of the references to colour in this figure legend, the reader is referred to the web version of this article.)

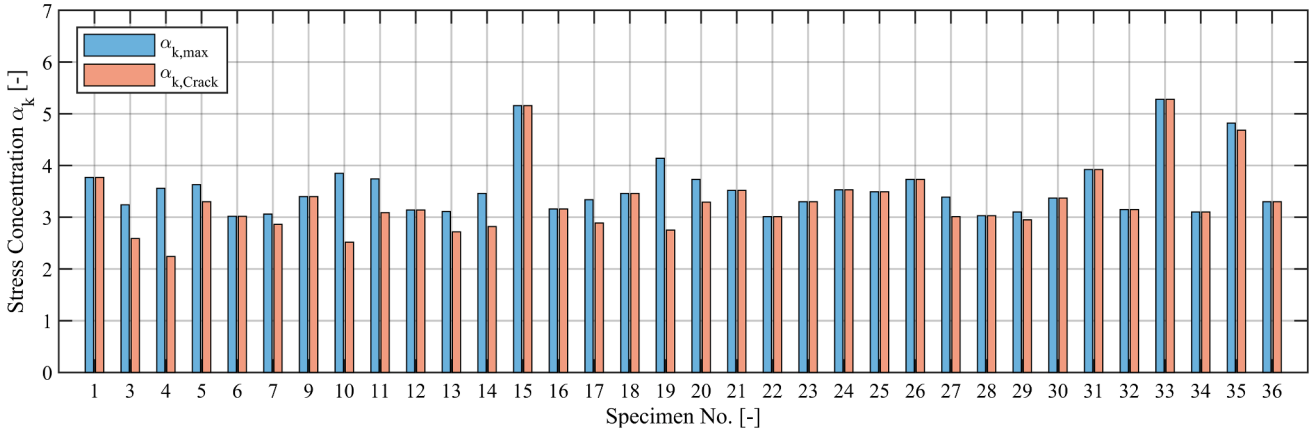

Fig. 22. Stress concentrations from numerical analysis of all specimens with corresponding stress concentrations at the crack location.

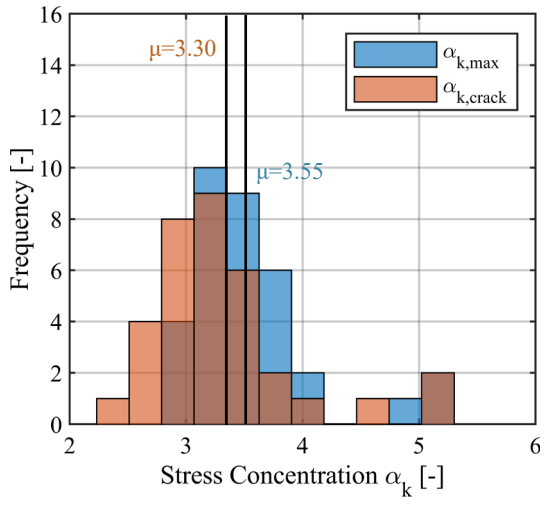

Fig. 23. Frequency plot of stress concentrations from numerical analyses of all specimens.

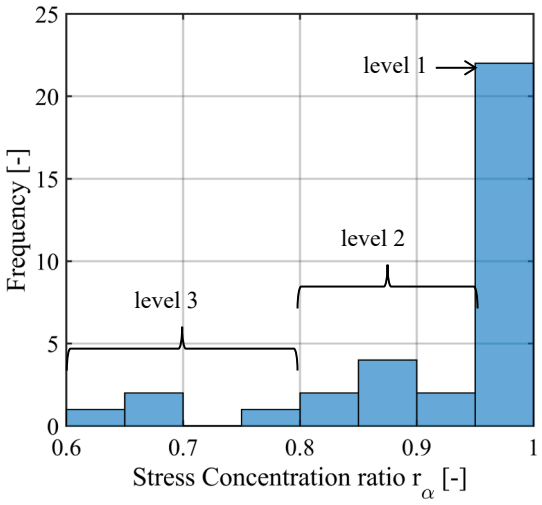

Fig. 24. Frequency plot of stress concentration ratio r_α.

effective notch stress radius of r = 1 mm, which is established in relevant codes [14,22]. However, none of them are applied to corroded steel yet. Nevertheless, in Fig. 25, the stress concentration of specimen No.5 is plotted for the max. stress concentration and the crack location along the thickness. The gradient at the max. stress location is slightly higher than at the crack location. At a distance of about 0.4 mm from the surface the stresses at the crack location are getting higher than at the max. stress location. This is in accordance with the research of Skallerud et. al. [56], where a averaged stress over a certain distance was found out to be the crack initiation site of rough surfaces. This underlines the impact of micro and macro structural support, which is an object of further research.

4.4. Findings

Following findings are described in this paper:

- The fatigue tests have shown a higher slope and higher fatigue life endurance compared to the corresponding DNV curve C-Air for rolled plates with pitting corrosion in Air.
- The fatigue life endurance for plates with pitting are higher than that of butt welds (category C1 and D, whether ground flushed or not).
- The notch effects can be analyzed by conversion of scan data into a numerical model with the aid of the reverse engineering method.
- The results of DIC enables the evaluation of the crack initiation life time. The average lifetime for steel plates with pitting corrosion is 88% of the total life time, based on a 2 mm crack length. The crack length has only little correlation with the stress range.
- There is a good match of DIC with the numerical prediction. For 13 of 21 specimen the crack locations coincide with the hotspot from numerical simulation.
- The notch effect has a leading impact on the crack location and crack path. Based on this finding, it is assumed, that the value of the stress concentration factor has an influence on the fatigue life endurance as well.
- In cases the crack location did not match with the max. stress concentration it was found that the stress gradients along the thickness was higher, which indicates a possible micro or macro support effect.

5 Conclusion

The objective for this paper was to investigate the fatigue behaviour of steel plates with pitting corrosion and identify the impact of local stress concentrations due to pitting in order to enable local fatigue life approaches for corroded components of offshore wind energy support

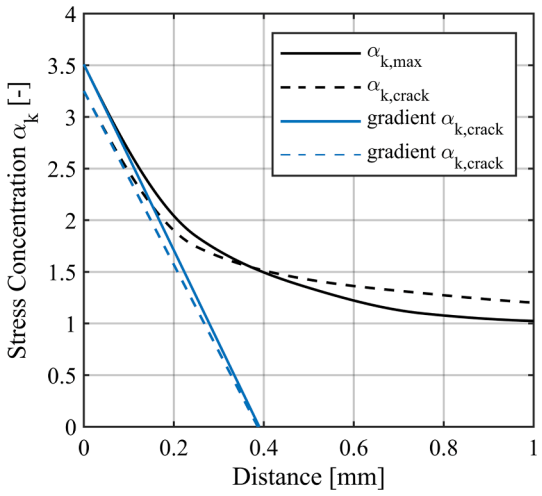

Fig. 25. Stress concentration along the thickness for max. stress concentration and crack location.

structures. With the aid of the reverse engineering method, it was shown that the stress concentration has a significant impact on the crack location and crack path. Nevertheless, in some specimens the max. stress concentrations were higher than at the actual crack location. This is assumed to be caused from the micro and macro structural support, which was not considered in the numerical simulation. The structural support has to be addressed in future research work. This becomes even more important, when calculating the fatigue life based on local approaches like e.g. the notch strain concept. For this purpose, the fatigue life data until crack initiation, conducted in this paper, can be used. Finally, with local fatigue approaches based on the reverses engineering method a differentiation between strongly notched components like tubular joints, which are not sensitive to stress concentration from pitting corrosion, and weakly notched components like welded plates can be made.

Declaration of Competing Interest

The authors declare that they have no known competing financial interests or personal relationships that could have appeared to influence the work reported in this paper.

Acknowledgements

The project ISyMOO is funded by the Federal Ministry of Economic Affairs and Climate Action (BMWK) through the 6th National Energy Research Program under the funding number 0324254A.

Ms. Mengyan Peng has contributed to this work within her Master thesis. This contribution is much appreciated.

Appendix A. Fatigue test data

Table 5
Fatigue test results.

Specimen No.	Max. load F_{max} [kN]	Min. load F_{min} [kN]	Load ratio R [-]	Cross section area A_{ave} [mm^2]	Stress range $\Delta\sigma$ [N/mm^2]	Fatigue life N_T [-]
P.01	105	10.5	0.1	403.5	234.2	313,070
P.02	40	4	0.1	364.5	98.8	2,000,000
P.03	90	9	0.1	391.5	206.9	417,736
P.04	100	10	0.1	388.2	231.8	320,864
P.05	80	8	0.1	404.1	178.2	699,371
P.06	115	11.5	0.1	402.3	257.3	187,517
P.07	70	7	0.1	372.4	169.2	1,664,437
P.08	65	6.5	0.1	406.8	143.8	8,387,846
P.09	115	11.5	0.1	421.5	245.6	205,740
P.10	115	11.5	0.1	404.8	255.7	79,200
P.11	115	11.5	0.1	395.3	261.8	93,357
P.12	90	9	0.1	379.9	213.2	542,572
P.13	90	9	0.1	391.6	206.8	597,934
P.14	90	9	0.1	411.0	197.1	795,004
P.15	75	7.5	0.1	361.2	186.9	315,444
P.16	80	8	0.1	398.9	180.5	1,661,456
P.17	80	8	0.1	405.5	177.5	1,432,112
P.18	80	8	0.1	406.4	177.2	1,427,084
P.19	80	8	0.1	407.5	176.7	898,498
P.20	80	8	0.1	390.9	184.2	832,000
P.21	115	11.5	0.1	413.1	250.6	178,651
P.22	90	9	0.1	387.9	208.8	266,790
P.23	115	57.5	0.5	405.1	141.9	1,339,331
P.24	125	62.5	0.5	406.8	153.7	988,000
P.25	130	65	0.5	407.8	159.4	690,454
P.26	130	65	0.5	414.3	156.9	1,497,211
P.27	130	65	0.5	404.1	160.8	947,958
P.28	130	65	0.5	385.4	168.6	880,362
P.29	130	65	0.5	394.7	164.7	983,877
P.30	130	65	0.5	414,6	156,8	411,240
P.31	80	−8	−0.1	420.1	209.5	622,036
P.32	80	−8	−0.1	400.0	220.0	435,103
P.33	80	−8	−0.1	422.6	208.2	341,448
P.34	80	−8	−0.1	404.4	217.6	403,782
P.35	80	−8	−0.1	402.9	218.4	281,212
P.36	80	−8	−0.1	398.7	220.7	556,415

Appendix B. Results of DIC measurements

Table 6
Results of DIC measurements.

Specimen No.	R [-]	Stress range $\Delta\sigma$ [N/mm^2]	Fatigue life total N_T [-]	Fatigue life N_{C1} [-]	Fatigue life N_{C2} [-]	Ratio r_{c1} N_{C1}/N_T	Ratio r_{c2} N_{C2}/N_T	Difference $\lvert N_{C1}-N_{C2}\rvert$	Crack length at N_{C1} [mm]
P.01	0.1	234.2	313,070	255,000	266,000	0.81	0.85	0.04	0.61
P.02	0.1	98.8	2,000,000	run out					
P.03	0.1	206.9	417,736	358,000	365,000	0.86	0.87	0.02	1.00
P.04	0.1	231.8	320,864	286,000	291,200	0.89	0.91	0.02	0.39
P.05	0.1	178.2	699,371	570,000	590,000	0.82	0.84	0.03	0.56
P.06	0.1	257.3	187,517	crack outside DIC frame					
P.07	0.1	169.2	1,664,437	1,520,000	1,560,000	0.91	0.94	0.02	0.47
P.08	0.1	143.8	8,387,846	run out					
P.09	0.1	245.6	205,740	126,000	144,000	0.61	0.70	0.09	0.84
P.10	0.1	255.7	79,200	crack outside DIC frame					
P.11	0.1	261.8	93,357	crack outside DIC frame					
P.12	0.1	213.2	542,572	476,000	506,000	0.88	0.93	0.06	0.80
P.13	0.1	206.8	597,934	crack outside DIC frame					
P.14	0.1	197.1	795,004	crack outside DIC frame					
P.15	0.1	186.9	315,444	230,000	270,000	0.73	0.86	0.13	0.91
P.16	0.1	180.5	1,661,456	1,290,000	1,312,000	0.78	0.79	0.01	0.68
P.17	0.1	177.5	1,432,112	1,362,000	1,400,000	0.95	0.98	0.03	0.45
P.18	0.1	177.2	1,427,084	1,320,000	1,354,000	0.92	0.95	0.02	0.92
P.19	0.1	176.7	898,498	crack outside DIC frame					
P.20	0.1	184.2	832,000	684,000	722,000	0.82	0.87	0.05	0.62
P.21	0.1	250.6	178,651	150,000	152,000	0.84	0.85	0.01	0.45
P.22	0.1	208.8	266,790	186,000	213,000	0.70	0.80	0.10	0.41
P.23	0.5	141.9	1,339,331	crack outside DIC frame					
P.24	0.5	153.7	988,000	crack outside DIC frame					
P.25	0.5	159.4	690,454	crack outside DIC frame					
P.26	0.5	156.9	1,497,211	crack outside DIC frame					
P.27	0.5	160.8	947,958	crack outside DIC frame					
P.28	0.5	168.6	880,362	crack outside DIC frame					
P.29	0.5	164.7	983,877	874,000	880,000	0.89	0.89	0.01	0.83
P.30	0.5	156,8	411,240	320,000	352,000	0.78	0.86	0.08	0.68
P.31	−0.1	209.5	622,036	crack outside DIC frame					
P.32	−0.1	220.0	435,103	350,000	380,000	0.80	0.87	0.07	0.11
P.33	−0.1	208.2	341,448	269,000	283,000	0.79	0.83	0.04	0.71
P.34	−0.1	217.6	403,782	310,000	332,000	0.77	0.82	0.05	1.01
P.35	−0.1	218.4	281,212	218,000	236,000	0.78	0.84	0.06	0.80
P.36	−0.1	220.7	556,415	440,000	480,000	0.79	0.86	0.07	0.96
				mean:		0.81	0.86	0.05	0.68
				standard deviation:		0.06	0.04	0.03	0.19
				5%-quantile		0.70	0.79	0.01	0.39
				95%-quantile		0.92	0.95	0.10	1.00

Appendix C. Results of numerical analysis

Table 7
Stress concentrations from numerical analysis.

Specimen No.	Load ratio R [-]	Stress range $\Delta\sigma$ [N/mm^2]	Stress concentration $\alpha_{k,\,max}$ [-]	Stress concentration $\alpha_{k,\,crack}$ [-]	Ratio $r_\alpha = \alpha_{k,\,crack}/\alpha_{k,\,max}$ [-]	Coincidance level [-]
P.01	0.1	234.2	3.77	3.77	1.00	level 1
P.03	0.1	206.9	3.24	2.59	0.80	level 2
P.04	0.1	231.8	3.56	2.24	0.61	level 3
P.05	0.1	178.2	3.63	3.30	0.92	level 2
P.06	0.1	257.3	3.02	3.02	1.00	level 1
P.07	0.1	169.2	3.06	2.86	0.92	level 2
P.09	0.1	245.6	3.40	3.40	1.00	level 1
P.10	0.1	255.7	3.85	2.52	0.65	level 3
P.11	0.1	261.8	3.74	3.09	0.79	level 2
P.12	0.1	213.2	3.14	3.14	1.00	level 1
P.13	0.1	206.8	3.11	2.72	0.83	level 2
P.14	0.1	197.1	3.46	2.82	0.81	level 2
P.15	0.1	186.9	5.16	5.16	1.00	level 1

(*continued on next page*)

Table 7 (*continued*)

Specimen No.	Load ratio R [-]	Stress range $\Delta\sigma$ [N/mm^2]	Stress concentration $\alpha_{k,\ max}$ [-]	Stress concentration $\alpha_{k,\ crack}$ [-]	Ratio r_α = $\alpha_{k,\ crack}/\ \alpha_{k,\ max}$ [-]	Coincidance level [-]
P.16	0.1	180.5	3.16	3.16	1.00	level 1
P.17	0.1	177.5	3.34	2.89	0.87	level 2
P.18	0.1	177.2	3.46	3.46	1.00	level 1
P.19	0.1	176.7	4.14	2.75	0.66	level 3
P.20	0.1	184.2	3.73	3.29	0.88	level 2
P.21	0.1	250.6	3.52	3.52	1.00	level 1
P.22	0.1	208.8	3.01	3.01	1.00	level 1
P.23	0.5	141.9	3.30	3.30	1.00	level 1
P.24	0.5	153.7	3.53	3.53	1.00	level 1
P.25	0.5	159.4	3.49	3.49	1.00	level 1
P.26	0.5	156.9	3.73	3.73	1.00	level 1
P.27	0.5	160.8	3.39	3.01	0.89	level 2
P.28	0.5	168.6	3.03	3.03	1.00	level 1
P.29	0.5	164.7	3.10	2.95	0.95	level 2
P.30	0.5	156.8	3.37	3.37	1.00	level 1
P.31	−0.1	209.5	3.92	3.92	1.00	level 1
P.32	−0.1	220.0	3.15	3.15	1.00	level 1
P.33	−0.1	208.2	5.28	5.28	1.00	level 1
P.34	−0.1	217.6	3.10	3.10	1.00	level 1
P.35	−0.1	218.4	4.82	4.68	0.97	level 2
P.36	−0.1	220.7	3.30	3.30	1.00	level 1
						Quantity
					Level 1:	20
					Level 2:	11
					Level 3:	3

References

[1] Det Norske Veritas. Corrosion protection for wind turbines(DNV-GL RP-0416); 2016.
[2] Federal Maritime and Hydrographic Agency. Minimum requirements concerning the constructive design of offshore structures within the Exclusive Economic Zone (EEZ); 2015.
[3] International Standards Organization. Corrosion of metals and alloys — Corrosivity of atmospheres: Classification, determination and estimation(ISO 9223:2012); 2012.
[4] Det Norske Veritas. Support structures for wind turbines(ST-0126); 2018.
[5] Cerit M. Corrosion pit-induced stress concentration in spherical pressure vessel. Thin-Walled Struct 2019;136:106–12. https://doi.org/10.1016/j.tws.2018.12.014.
[6] Liang X, Sheng J, Wang K. Investigation of the mechanical properties of steel plates with artificial pitting and the effects of mutual pitting on the stress concentration factor. Results Phys 2019;14:102520. https://doi.org/10.1016/j.rinp.2019.102520.
[7] Shojai S, Schaumann P, Brömer T. Probabilistic modelling of pitting corrosion and its impact on stress concentrations in steel structures in the offshore wind energy. Mar Struct 2022;84:103232. https://doi.org/10.1016/j.marstruc.2022.103232.
[8] Larrosa NO, Akid R, Ainsworth RA. Corrosion-fatigue: a review of damage tolerance models. Int Mater Rev 2018;63(5):283–308. https://doi.org/10.1080/09506608.2017.1375644.
[9] Xiang L, Pan J, Chen S. Analysis on the stress corrosion crack inception based on pit shape and size of the FV520B tensile specimen. Results Phys 2018;9:463–70. https://doi.org/10.1016/j.rinp.2018.03.005.
[10] Huang Y, Wei C, Chen L, Li P. Quantitative correlation between geometric parameters and stress concentration of corrosion pits. Eng Fail Anal 2014;44:168–78. https://doi.org/10.1016/j.engfailanal.2014.05.020.
[11] Hou J, Song L. Numerical investigation on stress concentration of tension steel bars with one or two corrosion pits. Adv Mater Sci Eng 2015;2015:1–7. https://doi.org/10.1155/2015/413737.
[12] Radaj D, Sonsino CM, Fricke W. Fatigue assessment of welded joints by local approaches. 2nd ed. Cambridge: Woodhead Publ. [u.a.]; 2006.
[13] Radaj D, Vormwald M. Advanced methods of fatigue assessment. Heidelberg: Springer; 2013.
[14] Hobbacher A. Recommendations for fatigue design of welded joints and components. IIW Document No. IIW-1823-07 International Institute of Welding; 2009.
[15] Fricke W. IIW recommendations for the fatigue assessment of welded structures by notch stress analysis. Oxford: WP Woodhead Publ; 2012.
[16] Sonsino CM, Fricke W, de Bruyne F, Hoppe A, Ahmadi A, Zhang G. Notch stress concepts for the fatigue assessment of welded joints – Background and applications. Int J Fatigue 2012;34(1):2–16. https://doi.org/10.1016/j.ijfatigue.2010.04.011.
[17] Ladinek M, Niederwanger A, Lang R, Schmid J, Timmers R, Lener G. The strain-life approach applied to welded joints: Considering the real weld geometry. J Constr Steel Res 2018;148:180–8. https://doi.org/10.1016/j.jcsr.2018.04.024.
[18] Lener G, Lang R, Ladinek M, Timmers R. A numerical method for determining the fatigue strength of welded joints with a significant improvement in accuracy. Procedia Eng 2018;213:359–73. https://doi.org/10.1016/j.proeng.2018.02.036.
[19] Braun M, Milaković A-S, Renken F, Fricke W, Ehlers S. Application of local approaches to the assessment of fatigue test results obtained for welded joints at sub-zero temperatures. Int J Fatigue 2020;138:105672.
[20] Schaumann P, Schürmann K, Pittner A, Rethmeier M. Automatically welded tubular X-joints for jacket substructures: prediction of the technical fatigue crack location. ce/papers 2019;3(3–4):823–8. https://doi.org/10.1002/cepa.1140.
[21] European Committee for Standardization. Eurocode 3 - Design of steel structures - Part 1-9: Fatigue(EN 1993-1-9); 2020.
[22] Det Norske Veritas - Germanischer Llyod. Fatigue design of offshore steel structures (DNV-GL RP-C203); 2019.
[23] Deutsches Institut für Normung e.V. Structures for wind turbines and platforms - Part 3: Steel structures(DIN 18088-3); 2019.
[24] Det Norske Veritas. Fatigue Assessment of Ship Structures(Classification Notes No. 30.7); 2014.
[25] Health & Safety Executive. Background to new fatigue guidance for steel joints and connections in offshore structures(OTH 92 390); 1998.
[26] Bundesanstalt für Wasserbau. Merkblatt: Bewertung der Tragfähigkeit bestehender Verschlüsse im Stahlwasserbau (TbVS); 2018.
[27] British Standards Institution. Guide to fatigue design and assessment of steel products(BS 7608:2014+A1:2015); 2014.
[28] Momber AW, Nattkemper TW, Langenkämper D, Möller T, Brün D, Schaumann P, et al. A data-based model for condition monitoring and maintenance planning for protective coating systems for wind tower structures. Renewable Energy 2022;186:957–73.
[29] Melchers R. A review of trends for corrosion loss and pit depth in longer-term exposures. Corros Mater Degrad 2018;1(1):42–58. https://doi.org/10.3390/cmd1010004.
[30] Revie RW, Uhlig HH. Corrosion and corrosion control: An introduction to corrosion science and engineering. Hoboken, New Jersey: Wiley-Interscience a John Wiley & Sons Inc. Publication; 2008.
[31] Marcus P. Corrosion mechanisms in theory and practice. 3rd ed. Boca Raton, Fla.: CRC Press; 2012.
[32] Le Li, Mojtaba Mahmoodian, Chun-Qing Li, Dilan Robert. Effect of corrosion and hydrogen embrittlement on microstructure and mechanical properties of mild steel.
[33] Mehmanparast A, Brennan F, Tavares I. Fatigue crack growth rates for offshore wind monopile weldments in air and seawater: SLIC inter-laboratory test results. Mater Des 2017;114:494–504. https://doi.org/10.1016/j.matdes.2016.10.070.
[34] Qvale P, Zarandi EP, Ås SK, Skallerud BH. Digital image correlation for continuous mapping of fatigue crack initiation sites on corroded surface from offshore mooring chain. Int J Fatigue 2021;151:106350. https://doi.org/10.1016/j.ijfatigue.2021.106350.
[35] Neumann KM, Ehlers S. Power spectrum for surface description of corroded ship structure from laser scan. In: Structures, safety, and reliability: Presented at ASME 2019 38th International Conference on Ocean, Offshore and Arctic Engineering,

June 9-14, 2019, Glasgow, Scotland, UK. New York, NY: The American Society of Mechanical Engineers; 2019.
[36] Nugroho FA, Braun M, Ehlers S. Probability analysis of PIT distribution on corroded ballast tank. Ocean Eng 2021;228:108958. https://doi.org/10.1016/j.oceaneng.2021.108958.
[37] G01 Committee. Practice for Preparing, Cleaning, and Evaluating Corrosion Test Specimens. West Conshohocken, PA: ASTM International. 10.1520/G0001-03R17E01.
[38] Biglu M. Doctoral Thesis - Effects of corrosion on the local behavior of steel structures under tensile loading.
[39] Friedrich N, Ehlers S. Crack monitoring in resonance fatigue testing of welded specimens using digital image correlation. J Visualized Experiments JoVE 2019; 151. https://doi.org/10.3791/60390.
[40] Radaj D, Vormwald M. Ermüdungsfestigkeit: Grundlagen für Ingenieure. 3rd ed. Berlin, Heidelberg: Springer-Verlag Berlin Heidelberg; 2007.
[41] Braun M, Fischer C, Baumgartner J, Hecht M, Varfolomeev I. Fatigue crack initiation and propagation relation of notched specimens with welded joint characteristics. Metals 2022;12(4):615. https://doi.org/10.3390/met12040615.
[42] ECCS European Convention for Constructional Steelwork. Background information on fatigue design rules: Statistical evaluation. 2nd ed. Brussels: ECCS European Convention for Constructional Steelwork; 2018.
[43] Friedrich N. Experimental investigation on the influence of welding residual stresses on fatigue for two different weld geometries. Fatigue Fract Eng Mater Struct 2020;65(3):128. https://doi.org/10.1111/ffe.13339.
[44] Hutt T, Cawley P. Feasibility of digital image correlation for detection of cracks at fastener holes. NDT and E Int 2009;42(2):141–9. https://doi.org/10.1016/j.ndteint.2008.10.008.
[45] Schürmann K. Fatigue Behavior of Automatically Welded Tubular Joints for Offshore Wind Energy Substructures. Dissertation 2021.
[46] Shojai, Sulaiman; Schaumann, Peter; Brömer, Tim (2022): Probabilistic modelling of pitting corrosion and its impact on stress concentrations in steel structures in the offshore wind energy. In: Marine Structures 84, S. 103232. DOI: 10.1016/j.marstruc.2022.103232.
[47] Basquin oh.. The exponential law of endurance tests. Proc Am Soc Test Mater 1910; 10:625–30.
[48] Deutsches Institut für Normung e.V. Load controlled fatigue testing – Execution and evaluation of cyclic tests at constant load amplitudes on metallic specimens and components(DIN 50100:2016-12). Berlin: Beuth Verlag GmbH; 2016.
[49] Murakami Y. Metal fatigue: Effects of small defects and nonmetallic inclusions. Amsterdam, London, San Diego, CA: Academic Press an imprint of Elsevier; 2019.
[50] Miller KJ. Initiation and growth rates of short fatigue cracks. Fundamentals of Deformation and Fracture 1984:477–500.
[51] Suresh S, Ritchie RO. Propagation of short fatigue cracks. Int Met Rev 1984;29(1): 445–75. https://doi.org/10.1179/imtr.1984.29.1.445.
[52] Collmann M. Ermüdungsfestigkeit von Stumpfnahtverbindungen größerer Blechdicke gefügt mit Hochleistungsschweißverfahren. Hannover Institutionelles Repositorium der Leibniz Universität Hannover 2021.
[53] Fatoba OO, Leiva-Garcia R, Lishchuk SV, Larrosa NO, Akid R. Simulation of stress-assisted localised corrosion using a cellular automaton finite element approach. Corros Sci 2018;137:83–97. https://doi.org/10.1016/j.corsci.2018.03.029.
[54] Turnbull A, Wright L, Crocker L. New insight into the pit-to-crack transition from finite element analysis of the stress and strain distribution around a corrosion pit. Corros Sci 2010;52(4):1492–8. https://doi.org/10.1016/j.corsci.2009.12.004.
[55] Taylor D. The theory of critical distances: A new perspective in fracture mechanics. Amsterdam, London: Elsevier; 2010.
[56] Skallerud B, Ås SK, Ottosen NS. A gradient-based multiaxial criterion for fatigue crack initiation prediction in components with surface roughness. Int J Fatigue 2018;117:384–95. https://doi.org/10.1016/j.ijfatigue.2018.08.020.